Research Article | Vol. 29, No. 5 / 1 March 2021 / Optics Express 7680
Optics EXPRESS

n-type Ge/Si antennas for THz sensing

C. A. Chavarin,[1,*] E. Hardt,[1] S. Gruessing,[2] O. Skibitzki,[1] I. Costina,[1] D. Spirito,[1] W. Seifert,[1] W. Klesse,[1] C. L. Manganelli,[1] C. You,[3] J. Flesch,[3] J. Piehler,[3] M. Missori,[4,5] L. Baldassarre,[1,5] B. Witzigmann,[2] and G. Capellini[1,6]

[1]IHP - Leibniz Institut fuer innovative Mikroelektronik, Im Technologiepark 25, 15236 Frankfurt (Oder), Germany
[2]University of Kassel, Wilhelmshoeher Allee 71, 34121 Kassel, Germany
[3]University of Osnabrueck, Barbarastrasse 11, 49076 Osnabrueck, Germany
[4]Institute for Complex Systems, National Research Council of Italy, P.le A. Moro 5, 00185 Roma, Italy
[5]Department of Physics, Sapienza University of Rome, P.le Aldo Moro 5, 00185 Roma, Italy
[6]Department of Sciences, Università degli Studi Roma Tre, Viale G. Marconi 446, 00154 Roma, Italy
*alvarado@ihp-microelectronics.com

Abstract: Ge-on-Si plasmonics holds the promise for compact and low-cost solutions in the manipulation of THz radiation. We discuss here the plasmonic properties of doped Ge bow-tie antennas made with a low-point cost CMOS mainstream technology. These antennas display resonances between 500 and 700 GHz, probed by THz time domain spectroscopy. We show surface functionalization of the antennas with a thin layer of α-lipoic acid that red-shifts the antenna resonances by about 20 GHz. Moreover, we show that antennas protected with a silicon nitride cap layer exhibit a comparable red-shift when covered with the biolayer. This suggests that the electromagnetic fields at the hotspot extend well beyond the cap layer, enabling the possibility to use the antennas with an improved protection of the plasmonic material in conjunction with microfluidics.

1. Introduction

Plasmonics, with its ability to manipulate light into sub-wavelength volumes, could help boosting performances and add functionalities to photonic devices operating in the THz range of the electromagnetic spectrum [1–3]. Indeed, one can exploit plasmonics in manipulating THz radiation, focusing it on subwavelength volumes and/or waveguiding [4]. Plasmon-polaritons, i.e. quasiparticles arising from light-matter interactions that yield strong field confinement and enhancement, can be sustained either by a metallic-dielectric interface (surface plasmon polaritons - SPPs) or localized by subwavelength metallic structures (localized surface plasmons - LSPs). In particular, LSP resonances can be engineered by structuring metals on a subwavelength scale and plasmonic meta-surfaces can be specifically designed to tailor the dispersion and the confinement of waves traveling along their surface. Alternatively, one can obtain strongly localized fields in the infrared and in the THz spectral range relying on doped semiconductors and conducting polymers [5,6]. Particularly, compared to metals, semiconductors have the advantage of a tunable plasma frequency by controlling their carrier concentration (N). In semiconductor-based plasmonic devices, negative permittivity is achieved over a wide frequency range below their screened plasma frequency ω_p^*, in the mid- and far-IR spectral range [7–13].

If, on one hand, III-V compound semiconductors (InP, GaAs) feature inherently higher carrier mobilities and thus can lead to lower plasmonic losses, on the other hand the use of elemental semiconductors opens up to the realization of mass-produced THz plasmonic devices. By leveraging on the low-point cost of Si-based CMOS mainstream technology, it is possible to

#418382 https://doi.org/10.1364/OE.418382
Journal © 2021 Received 24 Dec 2020; revised 10 Feb 2021; accepted 10 Feb 2021; published 25 Feb 2021

Optics EXPRESS

enable the widespread use of plasmonics in consumer products for different application realms. A further advantage of CMOS technology, specifically SiGe-based technologies, is the capability to monolithically realize a single platform comprising mixed-signal electronics, biosensors and microfluidics. These advantages are highly relevant for the implementation of Lab-on-a-chip devices which can profoundly impact the public health sector. Indeed, several applications in the medical field can be envisioned, such as point of care testing, owing to the non-ionizing nature of THz radiation [14]. Furthermore, the THz spectral range comprises the characteristic energies of molecular vibration, rotation, and libration, thus enabling e.g. environmental monitoring of volatile organic compounds [14,15]. Several Si-based or Si-compatible approaches have been reported in the literature for devices operating in the THz region, such as plasmonic antennas [16–19], cavities [20], particles [21], and gratings [22]. Aside from Si, in the past few years, Ge has entered routinely the CMOS foundry process flow, given the possibility to obtain high quality heteroepitaxial growth of Ge/Si structures that could be used for plasmonic applications. In fact, Ge has the advantage over Si of inherently lower losses [23], a lower electron effective mass [24], and can be doped with donor densities up to 10^{20} cm^{-3} [25]. Moreover, the use of doped Ge/Si heterostructures for the realization of resonators on Si substrates allows for a selective functionalization of Ge surfaces, in view of their application towards molecule sensing [26].

In this work, we demonstrate that THz bow-tie antennas fabricated using phosphorous-doped, n-type Ge/Si (001) can detect a deeply subwavelength layer of α- (Alpha-) Lipoic Acid (ALA) selectively absorbed on their surface. In order to assess the relevance of material quality on the plasmonic properties, we have investigated antennas made out of epitaxial doped Ge layers realized with different processes and featuring different electron mobility. By exploiting a CMOS-compatible manufactory pilot-line, we have realized several antenna array arrangements, in terms of geometry and density, either Si_3N_4 encapsulated or left bare. For the different antenna arrangements we observed well-defined transmittance resonance in the 0.3-0.9 THz spectral region, in good agreement with finite element Maxwell simulations. We also show that a deposited ALA layer causes a reproducible resonance red shift of ~20 GHz on antennas, demonstrating the sensing capability of our devices.

2. Growth, fabrication and characterization

We first discuss the realization of the n-type Ge/Si heterostructures and their material properties. The deposition of n-doped Ge layers on slightly p-doped Si substrates Si(001) wafers (200 *mm*) has been carried out using a ASM Epsilon 2000 lamp-heated reduced-pressure chemical vapor deposition (RPCVD) single wafer system. Si(001) wafers were cleaned by means of a wet-chemical process (Radio Corporation of America, RCA, solution with a subsequent HF step). After RCA cleaning, the hydrogen terminated Si(001) wafers were transferred into the RPCVD system and prebaked at 1000 $^{\circ}C$ in H_2 for 45 *s* to remove remaining native oxide and moisture. After the cleaning, an n-type 100-nm buffer layer was deposited. A first set of samples (*G1*) was realized by depositing a 1.5 μm thick n-doped Ge layer by RPCVD on top of the Si(001) wafers at a growth temperature of 350 $^{\circ}C$ and 80 *Torr* chamber pressure, using N_2 as carrier gas for the reactant GeH_4 and the doping PH_3 gases. As will be later discussed, we have selected 1.5 μm as our target thickness as a trade-off between a strong plasmonic response and a technologically-relevant material process. The Ge layer is plastically relaxed, has a surface roughness of approximately 1-2 nm, and a threading dislocation density in the 10^7 cm^{-2} range [27,28].

Since a constant doping profile as well as a high donor activation ratio can be disrupted during growth by the out-diffusion of P, dopant dimer formation, or clustering of dopants [23], we have characterized the P doping profile using a Time-of-flight Secondary Ion Mass Spectroscopy (ToF-SIMS) in a ToF-SIMS V from IONTOF. The depth profiles were acquired by sputtering with a Cs^+ ion beam with an energy of 500 eV over a 300 × 300 μm^2 area and analyzing with a $Bi_1{}^+$

Optics EXPRESS

beam with an energy of 25 keV over a $100 \times 100\ \mu m^2$ area. The results of ToF-SIMS (Fig. 1(a)) show a constant doping profile of $\sim 1.5 \times 10^{19}\ cm^{-3}$ along the entire thickness of the Ge layer. The measured donor concentration is in agreement with the nominal one, which we have selected as a trade-off between the highest possible density of activated donors (and, consequently, larger ω_p^*) and the quality of the material [27,28]. We remark here that we found an excellent thickness and doping homogeneity over different areas of the 200-*mm* wafer (Fig. 1(a), inset), as only a negligible decrease in dopants concentration is found at the edge of the wafer. A second set of samples (*G2*) was grown by adding a 30 *nm*–thick silicon nitride (Si_3N_4) encapsulation layer on n-Ge epilayers deposited using the same process of *G1*. The capping layer was deposited by a low-pressure CVD (LPCVD) batch reactor system using Bis(t-butylamino)silane (BTBAS) and was followed by annealing at 700 $^\circ C$ for 10 *s* in a rapid thermal annealing furnace system.

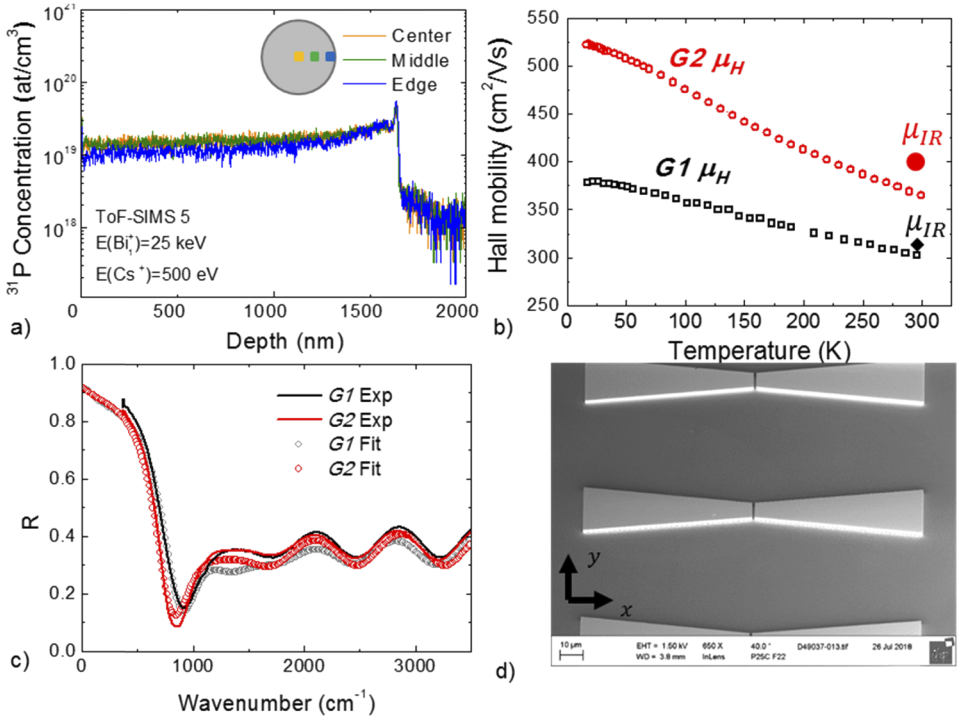

Fig. 1. (a) ToF-SIMS doping profile of a $\sim 1.6\ \mu m$ thick n-Ge layer. Inset: Analysis positions over the wafer. (b) Temperature sweep of Hall carrier mobility for *G1* and *G2* and comparison with mobility values extracted from Drude fitting of the FT-IR data. (c) Reflectivity measured between 500 and 3500 cm^{-1} for *G1* and *G2* compared to fitting based on Drude model. (d) SEM image of fabricated bow-tie n-Ge antennas in square arrangement.

Electrical transport characterization was carried out on representative sections of the n-Ge wafers for both *G1* and *G2*. A shadow mask was used to deposit an Al layer by sputtering, which is known to provide reliable electrical contacts to n-Ge [29]. Excellent agreement was found between four-point probe, van der Pauw and Hall bar contact scheme configurations, showing a low contact resistance. Additionally, temperature-dependent DC Hall measurements were performed. The contribution of the Si substrate carriers at low temperatures was removed thanks to the buried n-Si/p-Si isolating junction existing between the buffer layer and the substrate (see Supplement 1, Fig. S1(a) and S1(b)). In Fig. 1(b) the carrier mobility from Hall measurements (μ_H) at different temperatures is shown. At room temperature the Hall mobility was $\mu_H = 308\ cm^2/Vs$ for *G1* and $\mu_H = 370\ cm^2/Vs$ for *G2* sample, respectively. The mobility is in agreement

Optics EXPRESS

with model [30] and experimental [31] values in literature at room temperatures for bulk n-type Ge featuring similar concentrations. This points to the high quality of the material realized, in which the electron scattering process is dominated by that on phosphorous ion.

Fourier Transform Infrared (FT-IR) spectroscopy was performed in order to estimate the doping level and losses, and compare it to Hall data. Near-normal incidence reflectivity (R) measurements were performed at ambient conditions in a Bruker FTIR Vertex 80v with an A510/Q-T accessory using a gold mirror as reference. It is possible to identify clearly in the spectra the drop in reflectivity, corresponding to the screened plasma edge as well as oscillations arising from Fabry-Perot fringes within the Ge layer above the plasma edge. The experimental data was fitted by the transfer-matrix method (TMM) using the Drude model (Fig. 1(c)). Even though a generalized Drude approach would better describe the data [23], a simple Drude model, with a single scattering rate coefficient (γ) can reasonably describe room temperature data, yielding a doping concentration of $N_{IR} = 1.4{\times}10^{19}\ cm^{-3}$ and $N_{IR} = 1.2\times10^{19}\ cm^{-3}$ and a mobility of $\mu_{IR} = 310\ cm^2/Vs$ and $\mu_{IR} = 400\ cm^2/Vs$ for *G1* and *G2*, respectively, in reasonable agreement with Hall measurements.

We have then used these material data to feed the modeling of single antenna structures carried out using Finite Element Method (FEM) on an unstructured mesh [32,33] to obtain 3D vectorial solutions of the Maxwell equations. Starting from fixed values of doping N and mobility μ ($N = 1.5{\times}10^{19}\ cm^{-3}$ and $\mu = 310\ cm^2/Vs$) two different geometries, slab (dipole) vs bow-tie, were investigated, finding that for a target resonance frequency of 0.5 THz the extinction coefficient of the bow-tie geometry has a superior performance (>20%) against a simple slab geometry (see Supplement 1, Fig. S2). The gap width of 1 μm has been chosen for maximum field enhancement at the one hand, and reasonable size for sample loading and future microfluidic integration on the other hand (see [32]). Moreover, we have evaluated the behavior of the penetration depth $\delta(f) = \sqrt{1/\pi f \mu\sigma(f)}$, where $\sigma(f)$ is the frequency-dependent conductivity. For the above-mentioned values of doping and mobility, the penetration depth was calculated to be δ (0.5 THz) $\simeq 3.4\ \mu m$. As it will be later shown, we can nevertheless obtain a reasonably strong and narrow resonance in the plasmonic antennas made of both *G1* and *G2* materials.

Antennas were fabricated by employing 210 *nm* low-deposition rate silane-based silicon oxide (SiO_2) as a hard mask. After lithographic patterning (i-liner process), reactive ion etching was used to obtain the final antenna shape (see Fig. 1(d)). The bow-tie resonator has 74 μm as the length of each (trapezoid) arm, 30 μm (10 μm) for the base (apex) of the trapezoid and 1 μm as the antenna gap. In order to better tailor the antenna response, we realized antenna arrays with different primitive cells, namely square (*Sq*), hexagonal (*Hx*) and a random (*Rd*) array (see Supplement 1, Fig. S3). For each array, samples have been fabricated with various antenna distances, as summarized in Table 1. For the fabrication of antennas on the *G2* material an additional process step after wet chemistry was used. This consisted of 30 *nm* Si_3N_4 additionally deposited by LPCVD batch reactor system using BTBAS, in order to cover the sidewalls and top of the created resonator structures for a final thickness of 30 *nm* and 60 *nm* Si_3N_4, respectively.

Table 1. Antenna-to-antenna separation for the different arrays studied.

Design	*Sq-A*	*Sq-B*	*Sq-C*	*Hx-A*	*Hx-B*	*Hx-C*
X-Distance (μm)	450	290	210	450	290	210
Y-Distance (μm)	330	180	90	640	330	175

3. Antennas and sensing

Antennas extinction have been obtained by means of Terahertz Time Domain Spectroscopy (THz-TDS), with a spectral bandwidth of 5 THz, 90 dB dynamic range and a frequency resolution

Optics EXPRESS

of less than 1.2 GHz (Terasmart from Menlo Systems, Germany and TERA K15 all-fiber coupled THz spectrometer from Menlo Systems, Germany [34]). In the TERA K15 systems the THz emission were obtained by photoconductive antennas excited by a femtosecond fiber-coupled laser (Menlo Systems T-Light) with center wavelength of 1560 nm, 100 MHz repetition frequency, and a pulse duration of nearly 90 fs [35]. The THz radiation emitted by the photoconductive antenna was collected and collimated by means of a TPX (polymethylpentene) lenses. The samples were placed at the THz focus where the illuminated area was approximately 3 *mm* in diameter, so that the THz pulse could probe a large area, thus minimizing heterogeneity effects. Fabry-Perot interference effects were removed from spectral data by a numerical procedure [34]. Measurements were performed in a transmission setup with a linearly polarized source. Spectra were collected by aligning the long axis of the antenna arms parallel to the electric field polarization ($I_{\parallel}$), thus exciting the antenna resonance, and, as reference, with the long antenna axis perpendicular to the electric field polarization ($I_{\perp}$). Measurements were performed in air. In order to eliminate the contribution of water absorption lines due to the environmental humidity, measurements of $I_{\parallel}$ and $I_{\perp}$ were carried out quickly one after the other (both acquisitions in less than 5 minutes). This ensured for a small variation of the humidity and a very good compensation of water absorption lines in the dichroic ratio obtained as DR=-ln($I_{\parallel}/I_{\perp}$). The dichroic ratio obtained is plotted in Fig. 2, showing a clear antenna resonance. Moreover, we also have measured a bare Si substrate as reference, in order to calculate the transmittance for the two polarizations of the electric field (Supplement 1, Fig. S4). In Fig. 2(a) we compare the experimental data with the theoretical calculations obtained for an increasing density of antennas (*A, B, C*), as well as for different antenna arrangements (*Hx, Sq*).

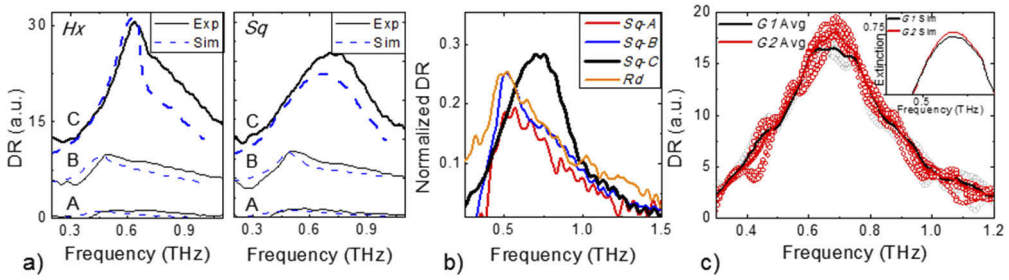

Fig. 2. (a) Experimental (solid lines) and TFSF simulations (dashed lines) of *G1* THz resonance for increasing antenna density (*A, B, C*) in a *Hx* and *Sq* arrangements. (b) Dichroic ratio for increasing antenna density in *Sq* arrangement compared to random antenna arrangement normalized by the number of antennas. (c) Experimental and (inset) FEM simulation comparison of *G1* and *G2* THz resonances.

The resonant frequency of the sample with the highest antenna density (*C*) displays a blue shift, when compared to the designed single antenna center frequency, as a result of antenna-to-antenna cross-talk (see Fig. 2(b), where the dichroic ratio has been normalized to the number of antennas in the THz focal spot). Indeed, the antenna resonance measured for larger antenna spacing (*A* and *B*) is comparable to that found when the antennas are placed on a random pattern. Mutual coupling between individual neighboring antennas and their near-fields thus results in shifted spectra [36,37]. The theoretical simulations were adjusted to account for inter-antenna interactions within the array by treating each antenna as a scatterer in a total field scattered field (TFSF) approach. This resulted in a good agreement with the experimental data, demonstrating the capacity of the model to accurately predict the THz behavior.

We have, moreover, collected the experimental data from 10 replicas of *G1* (gray circles) and *G2* (red circles) sample from different parts of the 200 *mm* wafers showing high reproducibility throughout the wafer (Fig. 2(c)). A small difference was found, by averaging all data collected

Optics EXPRESS

on each wafer among *G1* and *G2* antennas. To understand whether a small effect of mobility on the resonance can be seen we compared qualitatively with simulations (inset in Fig. 2(c)). Indeed simulations, where only the mobility difference among *G1* and *G2* was taken into account, show a comparable effect on the resonance, while the presence of the Si_3N_4 capping layer was disregarded.

To demonstrate the sensing capability of our devices, we then explored selective functionalization of the Ge layers with α-lipoic acid (ALA). The intramolecular disulfide group of ALA mediates selective covalent bonding to the Ge surface while the remaining carboxyl moiety is suitable for immobilization of biomolecules. We have previously shown self-assembly of ALA monolayers on freshly cleaned Ge surfaces, which are stabilized by germanium-sulfur bonds [26]. In a process previously reported [26], the native oxides and/or residual contaminants are removed from the Ge surface by a HF (12%)/H_2O_2 (7%) cyclic cleaning procedure. To avoid possible etching effects and surface roughness, citric acid was used instead as an alternative for the removal of the native oxide [38]. The H-passivated surfaces are then incubated in an ethanol/DI water/ALA solution (5 mM, pH 6) overnight at $4°C$. Under these conditions ALA forms a multilayer with a well-defined thickness of at least 20 nm [26].

The effect of ALA adlayer formation on the antennas is detected as a red-shift of the antennas resonances (Fig. 3(a) and 3(b)), which is comparable for both *G1* and *G2*. Data were fitted with a Gaussian line shape to better estimate the central frequency. The resonances for both *G1* and *G2* are centered at about 0.7 THz before the incubation of ALA (in red). After the incubation period (in black), both show a red shift of about 20 GHz and a reduction of the resonance intensity of about 10%. In Fig. 3(c), we show simulations of the resonance behavior to the presence of a material, with varying refractive index (n), completely filling the antenna-gap and a 100 nm thick layer (lower value allowed by simulations) on its surface and rear-end of the antennas. Interestingly, the red shift of the resonance due to the ALA layer, if compared to the identical clean sample as reference, confirms the sensitivity of the plasmonic resonance to changes in their dielectric environment. The observed experimental red-shift qualitatively agrees with the simulations of a 100 nm layer ($n > 1$) covering the antennas and filling the 1 μm antenna-gap, suggesting a value of $n \sim 1.5$ for the ALA layer at this frequency. These results are in complete agreement with the expected sensing behavior of the resonators. Within the antenna gap, the fields are concentrated and enhanced by orders of magnitude, making this volume the most responsive part of the sensor to the material therein.

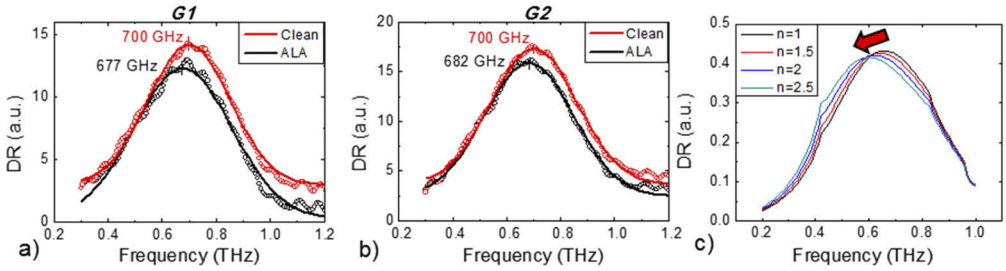

Fig. 3. Experimental results (unfilled circles) and Gaussian fit (solid lines) of (a) *G1* and (b) *G2* before (red) and after (black) ALA incubation. (c) Simulation results of the effect on the resonance caused by a film covering the whole gap and 100 nm surface of the antennas at different n values.

The identical center frequency between *G1* and *G2* antennas, i.e. one with the Si_3N_4 encapsulation, may stem from a combination of factors. First of all, despite a full coverage, the Si_3N_4 is thinner on the sidewalls than on the antenna surface. The enhanced fields arising due to the LSP resonance are mainly located along the antenna feed gap, and as the gap is filled by the

Optics EXPRESS

Si_3N_4 only by a small percentage of the entire volume it can result in the aforementioned behavior. Interestingly, the red-shift due to the presence of ALA is comparable in the two samples, despite the presence of Si_3N_4. Again, the behavior can be understood as the main field interaction takes place within the gap volume from which the thin encapsulation layer has a negligible effect on the antenna response. While we expect the field enhancement at the hot spot to exceed the Si_3N_4 thickness, ALA binding on the surface of the encapsulation layer was not given for granted.

To thoroughly confirm the presence of the biolayer and its distribution on the antennas, a set of measurements consisting of nano-Auger Electron Spectroscopy (AES), ToF-SIMS and X-ray Photoelectron Spectroscopy (XPS) were performed in incubated and reference samples. AES mapping were performed using a Physical Electronics PHI 670 type Scanning Auger Microprobe with an electron energy of 10 keV by acquiring the Ge, Si and S signals with 256 pixel x 256 pixel resolution. AES maps of the characteristic signals of Ge, Si and S for an incubated sample are shown in Fig. 4(a), 4(b) and 4(c), respectively. The presence of sulfur confirms the binding of ALA on the antenna's surface. Indeed, thanks to the high resolution and surface sensitivity of AES measurements it is possible to show the presence of an S-containing layer in the incubated samples (Fig. 4(c)). The observed behavior can be explained by the anticipated ALA selectivity to Ge against SiO_2 [26]. Even though the Si substrate was not deliberately oxidized, a native oxide can be expected in the surface of Si (see the O signal in Supplement 1, Fig. S5). By comparing the maps obtained for Ge and Si, clearly showing the gap between antennas, with the map obtained for S distribution we can infer an accumulation of S in the gap, which rules out any wettability problem of the hotspot region.

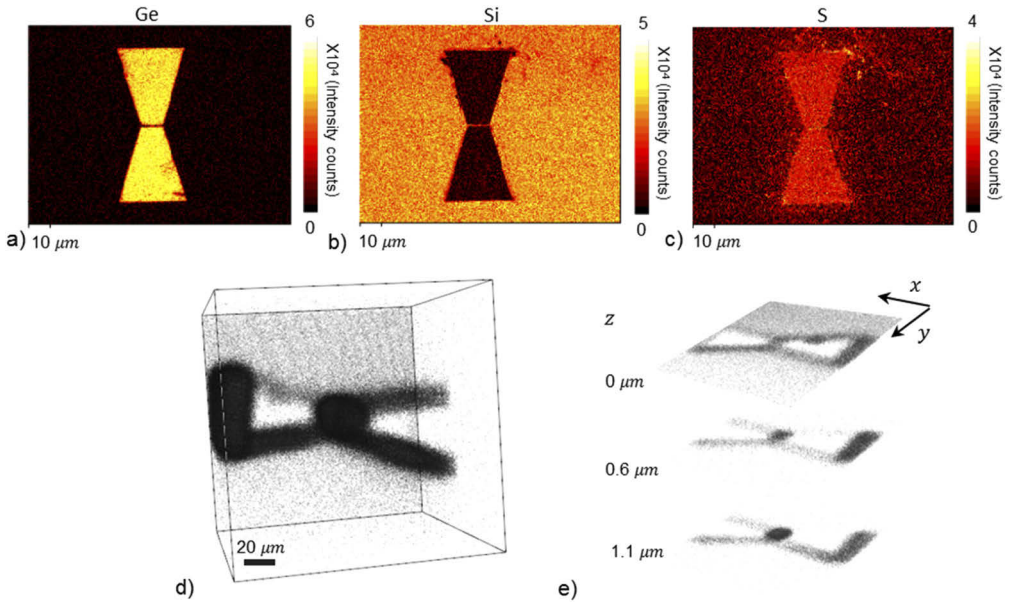

Fig. 4. (a) Germanium, (b) silicon and (c) sulfur AES maps of *G1* ALA-treated samples. (d) 3D ToF-SIMS reconstruction and (e) sliced view at different heights showing the S concentration around one Ge antenna and especially in the gap.

In order to visualize the 3D distribution of ALA, depth profiles were measured by ToF-SIMS using S^- ions as the marker for lipoic acid. The S accumulation, and thus the ALA binding to the antenna, is more clear in the 3D reconstruction of ToF-SIMS measurement (Fig. 4(d) and 4(e)) where it is noticeable that sulfur (seen as black shade) tends to accumulate at the edges (walls) and gap of the antenna. It can be seen that the presence of sulfur is distributed over the antenna

Optics EXPRESS

and substrate surface at the beginning of the Tof-SIMS experiments (Fig. 4(e), 0 μm). As the sputtering continues (Fig. 4(e), 0.6 and 1.1 μm) the S signal is mostly coming from the gap and walls. This suggest that surface tension between the ALA solution and the antenna structure, as the liquid dries out after incubation, allows for an effective coverage of the antenna walls, also in the feed gap. The apparent higher signal of S on one antenna side of the ToF-SIMS results shown in Fig. 4(d) can be explained as an artifact produced by the 45° inclination of the sputtering gun with respect to the detector, giving the impression of a preferential side. Furthermore, a low ion energy (250 eV) was used to slowly sputter the sample's surface and follow the component concentration along the depth profile. ToF-SIMS highest mass resolution settings were used to confirm and avoid crosstalk between the S and (2x) oxygen signal.

The XPS analysis of reference and ALA-treated samples for both generations were acquired in a Ulvac-PHI VersaProbe II instrument equipped with a monochromatic Al K-Alpha X-ray source with a photoelectron takeoff angle of 45°, a hemispherical analyzer and Argon ion gun. A dual-beam charge neutralizer (8 eV Ar$^+$ and 10 eV-electron beam) was used to compensate the charge-up effect. The measurements were performed using a pass energy of 29 eV in order to ensure a good energy resolution. As expected, the XPS spectra in Fig. 5(c) shows the intrinsic differences of (bare Ge) *G1* and (Si_3N_4 encapsulated) *G2* surfaces in their respective Ge and N signals. The complete absence of the Ge $2p_{3/2}$ and Ge 3d signals on *G2* samples demonstrated the effective encapsulation by the Si_3N_4. Similarly, the presence of the S 2p peak in ALA-treated samples (red lines) for both generations and its absence in the reference sample (blue lines), corroborate the existence of a shallow sulfur-containing layer on their surfaces. While the complete coverage of Ge atoms would hinder the binding of ALA, it can be expected that during the pretreatment and/or incubation procedure, the Si_3N_4 layer can at least partially oxidize in its surface [39]. These would produce Si/SiO_x sites for the binding with ALA, which albeit being less effective than bare Ge, is nevertheless present (Fig. 4(c)). The measurements here presented endorse the non-selective binding of the biolayer to the encapsulated Ge antennas. The encapsulation layer is shown to have a minimum effect in its sensing capabilities which not only allows to improve the plasmonic material properties but also increases its robustness against aqueous solutions in microfluidic applications.

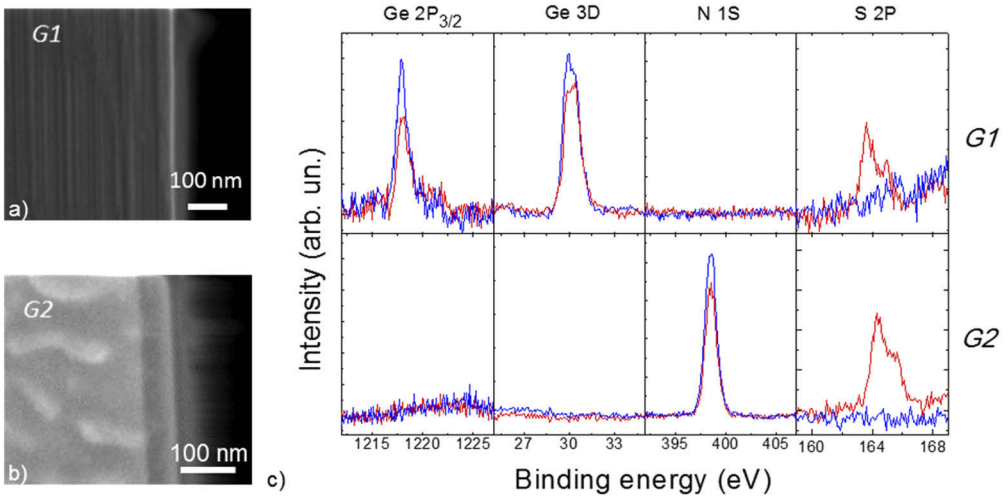

Fig. 5. SEM lateral view of (a) *G1* and (b) *G2* ALA-treated samples. (c) Germanium, nitrogen and sulfur XPS spectra of reference (in blue) and ALA-treated (in red) samples.

Optics EXPRESS

In SEM images with lateral view of *G1* and *G2* incubated samples, a ~20 *nm*-thick layer can be distinguished for both generations (Fig. 5(a) and Fig. 5(b), respectively), in agreement with the results of the above-mentioned measurements and those of Kazmierck et al. [26]. The visible streaking of the outmost layer in Fig. 5(b) can be seen as an artifact influenced by the non-conductive Si_3N_4 layer. Taking in consideration the vacuum conditions required for the characterization techniques mentioned above, a range, as an upper limit, for the thickness of the incubated ALA layer can be set between ~100 *nm* and ~1 μm given that the devices were kept in atmospheric conditions during the THz-TDS experiments. Indeed an extended exposure to atmospheric and/or vacuum conditions could influence the stability of the ALA layer. Such thickness range of the biolayer would in any case correspond to a non-specific subwavelength detection by the Ge resonant antennas between two and three orders of magnitude.

4. Conclusions

CMOS-compatible THz plasmonic antennas were fabricated in a pilot fabrication line. Up to 1.5 μm of highly n-doped Ge layers with a high carrier activation and mobility of up to 370 cm^2/Vs were grown epitaxially on Si (001) substrates. Ge antennas show a strong, polarization dependent resonance at 0.5-0.7 THz that were probed for several geometric shapes and periodic arrangements. We have shown that it is possible to bind a layer of α-Lipoic Acid selectively on Ge surfaces and sense it via a resonance shift. This is as well observed for antennas protected with a Si_3N_4 cap layer. These findings pave the way towards the possibility of achieving selective molecule bindings for microfluidic applications on a fully CMOS compatible sensing platform.

Funding. Deutsche Forschungsgemeinschaft (ESSENCE, SPP-1857 priority program).

Acknowledgments. The authors wish to thank M.Sc. Felix Reichmann and Dr. Marvin Zoellner for the fruitful discussions in the interpretation of XPS data. L.B. thanks the support of IHP's international "Wolfgang Mehr" fellowship award.

Disclosures. The authors declare that there are no conflicts of interest related to this article.

Supplemental document. See Supplement 1 for supporting content.

References

1. S. Enoch and N. Bonod, *Plasmonics: From Basics to Advanced Topics*, Springer Series in Optical Sciences (Springer, 2012).
2. Y. Lee, *Principles of Terahertz Science and Technology*, Lecture Notes in Physics (Springer, 2009).
3. D. M. Mittleman, "Frontiers in terahertz sources and plasmonics," Nat. Photonics **7**(9), 666–669 (2013).
4. X. Zhang, Q. Xu, L. Xia, Y. Li, J. Gu, Z. Tian, C. Ouyang, J. Han, and W. Zhang, "Terahertz surface plasmonic waves: a review," Adv. Photonics **2**, 1–19 (2020).
5. R. Soref, J. Hendrickson, and J. W. Cleary, "Mid- to long-wavelength infrared plasmonic-photonics using heavily doped n-Ge/Ge and n-GeSn/GeSn heterostructures," Opt. Express **20**(4), 3814–3824 (2012).
6. G. V. Naik, V. M. Shalaev, and A. Boltasseva, "Alternative plasmonic materials: Beyond gold and silver," Adv. Mater. **25**(24), 3264–3294 (2013).
7. S. Law, R. Liu, and D. Wasserman, "Doped semiconductors with band-edge plasma frequencies," J. Vac. Sci. Technol., B: Nanotechnol. Microelectron.: Mater., Process., Meas., Phenom. **32**(5), 052601 (2014).
8. G. V. Naik, J. L. Schroeder, X. Ni, A. V. Kildishev, T. D. Sands, and A. Boltasseva, "Titanium nitride as a plasmonic material for visible and near-infrared wavelengths," Opt. Mater. Express **2**(4), 478–489 (2012).
9. B. Dastmalchi, P. Tassin, T. Koschny, and C. M. Soukoulis, "A new perspective on plasmonics: Confinement and propagation length of surface plasmons for different materials and geometries," Adv. Opt. Mater. **4**(1), 177–184 (2016).
10. G. Pellegrini, L. Baldassare, V. Giliberti, J. Frigerio, K. Gallacher, D. J. Paul, G. Isella, M. Ortolani, and P. Biagioni, "Benchmarking the use of heavily doped Ge for plasmonics and sensing in the mid-infrared," ACS Photonics **5**(9), 3601–3607 (2018).
11. J. Chochol, K. Postava, M. Cada, M. Vanwolleghem, M. Micica, L. Halagacka, J.-F. Lampin, and J. Pištora, "Plasmonic behavior of III-V semiconductors in far-infrared and terahertz range," J. Eur. Opt. Soc. Publ. **13**(1), 13 (2017).
12. L. Baldassarre, E. Sakat, J. Frigerio, A. Samarelli, K. Gallacher, E. Calandrini, G. Isella, D. J. Paul, M. Ortolani, and P. Biagioni, "Midinfrared plasmon-enhanced spectroscopy with germanium antennas on silicon substrates," Nano Lett. **15**(11), 7225–7231 (2015).

Optics EXPRESS

13. H. Chong, Z. Xu, Z. Wang, J. Yu, T. Biesner, M. Dressel, L. Wu, Q. Li, and H. Ye, "CMOS-compatible antimony-doped germanium epilayers for mid-infrared low-loss high-plasma-frequency plasmonics," ACS Appl. Mater. Interfaces **11**(21), 19647–19653 (2019).
14. J.-H. Son, S. J. Oh, and H. Cheon, "Potential clinical applications of terahertz radiation," J. Appl. Phys. **125**(19), 190901 (2019).
15. N. Rothbart, H.-W. Hübers, K. Schmalz, J. Borngräber, and D. Kissinger, "Towards breath gas analysis based on millimeter-wave molecular spectroscopy," Frequenz **72**(3-4), 87–92 (2018).
16. A. Berrier, R. Ulbricht, M. Bonn, and J. G. Rivas, "Ultrafast active control of localized surface plasmon resonances in silicon bowtie antennas," Opt. Express **18**(22), 23226–23235 (2010).
17. A. Berrier, P. Albella, M. A. Poyli, R. Ulbricht, M. Bonn, J. Aizpurua, and J. G. Rivas, "Detection of deep subwavelength dielectric layers at terahertz frequencies using semiconductor plasmonic resonators," Opt. Express **20**(5), 5052–5060 (2012).
18. A. Berrier, M. C. Schaafsma, G. Nonglaton, J. Bergquist, and J. G. Rivas, "Selective detection of bacterial layers with terahertz plasmonic antennas," Biomed. Opt. Express **3**(11), 2937–2949 (2012).
19. G. Georgiou, H. K. Tyagi, P. Mulder, G. J. Bauhuis, J. J. Schermer, and J. G. Rivas, "Photo-generated THz antennas," Sci. Rep. **4**(1), 3584 (2015).
20. W. Withayachumnankul, C. M. Shah, C. Fumeaux, B. S.-Y. Ung, W. J. Padilla, M. Bhaskaran, D. Abbott, and S. Sriram, "Plasmonic resonance toward terahertz perfect absorbers," ACS Photonics **1**(7), 625–630 (2014).
21. M. C. Schaafsma, G. Georgiou, and J. G. Rivas, "Enhanced THz extinction in arrays of resonant semiconductor particles," Opt. Express **23**(19), 24440–24455 (2015).
22. S. Li, M. M. Jadidi, T. E. Murphy, and G. Kumar, "Terahertz surface plasmon polaritons on a semiconductor surface structured with periodic V-grooves," Opt. Express **21**(6), 7041–7049 (2013).
23. J. Frigerio, A. Ballabio, G. Isella, E. Sakat, G. Pellegrini, P. Biagioni, M. Bollani, E. Napolitani, C. Manganelli, M. Virgilio, A. Grupp, M. P. Fischer, D. Brida, K. Gallacher, D. J. Paul, L. Baldassarre, P. Calvani, V. Giliberti, A. Nucara, and M. Ortolani, "Tunability of the dielectric function of heavily doped germanium thin films for mid-infrared plasmonics," Phys. Rev. B **94**(8), 085202 (2016).
24. P. Biagioni, J. Frigerio, A. Samarelli, K. Gallacher, L. Baldassarre, E. Sakat, E. Calandrini, R. W. Millar, V. Giliberti, G. Isella, D. J. Paul, and M. Ortolani, "Group-IV midinfrared plasmonics," J. Nanophotonics **9**(1), 093789 (2015).
25. G. Scappucci, G. Capellini, W. M. Klesse, and M. Y. Simmons, "New avenues to an old material: controlled nanoscale doping of germanium," Nanoscale **5**(7), 2600–2615 (2013).
26. M. Kazmierczak, J. Flesch, J. Mitzloff, G. Capellini, W. M. Klesse, O. Skibitzki, C. You, M. Bettenhausen, B. Witzigmann, J. Piehler, T. Schroeder, and S. Guha, "Stable and selective self-assembly of alpha-lipoic acid on Ge(001) for biomolecule immobilization," J. Appl. Phys. **123**(17), 175305 (2018).
27. Y. Yamamoto, M. R. Barget, G. Capellini, N. Taoka, M. Virgilio, P. Zaumseil, A. Hesse, T. Schroeder, and B. Tillack, "Photoluminescence of phosphorous doped Ge on Si (100)," Mater. Sci. Semicond. Process. **70**, 111–116 (2017).
28. M. R. Barget, M. Virgilio, G. Capellini, Y. Yamamoto, and T. Schroeder, "The impact of donors on recombination mechanisms in heavily doped Ge/Si layers," J. Appl. Phys. **121**(24), 245701 (2017).
29. K. Gallacher, P. Velha, D. J. Paul, I. MacLaren, M. Myronov, and D. R. Leadley, "Ohmic contacts to n-type germanium with low specific contact resistivity," Appl. Phys. Lett. **100**(2), 022113 (2012).
30. C. Hilsum, "Simple empirical relationship between mobility and carrier concentration," Electron. Lett. **10**(13), 259–260 (1974).
31. M. J. Katz, "Electrical conductivity in heavily doped n-type germanium: Temperature and stress dependence," Phys. Rev. **140**(4A), A1323–A1344 (1965).
32. M. Bettenhausen, F. Romer, B. Witzigmann, J. Flesch, R. Kurre, S. Korneev, J. Piehler, C. You, M. Kazmierczak, S. Guha, G. Capellini, and T. Schroder, "Germanium plasmon enhanced resonators for label-free terahertz protein sensing," Frequenz **72**(3-4), 113–122 (2018).
33. F. Römer, B. Witzigmann, O. Chinellato, and P. Arbenz, "Investigation of the purcell effect in photonic crystal cavities with a 3D finite element Maxwell solver," Opt. Quantum Electron. **39**(4-6), 341–352 (2007).
34. R. Fastampa, L. Pilozzi, and M. Missori, "Cancellation of Fabry-Perot interference effects in terahertz time-domain spectroscopy of optically thin samples," Phys. Rev. A **95**(6), 063831 (2017).
35. M. D. Astorino, R. Fastampa, F. Frezza, L. Maiolo, M. Marrani, M. Missori, M. Muzi, N. Tedeschi, and A. Veroli, "Polarization-maintaining reflection-mode THz time-domain spectroscopy of a polyimide based ultra-thin narrow-band metamaterial absorber," Sci. Rep. **8**(1), 1985 (2018).
36. L. Zhao, K. L. Kelly, and G. C. Schatz, "The extinction spectra of silver nanoparticle arrays: influence of array structure on plasmon resonance wavelength and width," J. Phys. Chem. B **107**(30), 7343–7350 (2003).
37. R. Adato, A. A. Yanik, J. J. Amsden, D. L. Kaplan, F. G. Omenetto, M. K. Hong, S. Erramilli, and H. Altug, "Ultra-sensitive vibrational spectroscopy of protein monolayers with plasmonic nanoantenna arrays," Proc. Natl. Acad. Sci. **106**(46), 19227–19232 (2009).
38. G. Collins, D. Aureau, J. D. Holmes, A. Etcheberry, and C. O'Dwyer, "Germanium oxide removal by citric acid and thiol passivation from citric acid-terminated Ge(100)," Langmuir **30**(47), 14123–14127 (2014).
39. N. Banerji, J. Serra, P. Gonzalez, S. Chiussi, E. Parada, B. Leon, and M. Perez-Amor, "Oxidation processes in hydrogenated amorphous silicon nitride films deposited by ArF laser-induced CVD at low temperatures," Thin Solid Films **317**(1-2), 214–218 (1998).